



## REPORT

# Prandtl-Meyer Expansion over a 15-degree corner at Mach 2.5

Poomurugan C, Sameem Nazir Lone, Rajesh Ranjan\*

\*Corresponding author. Email: rajeshr@iitk.ac.in

### Abstract

In this study, our goal is to utilize a pre-developed "PRAVAH" solver to simulate the Prandtl-Meyer expansion wave over a 15-degree corner. Our objective is to validate our simulation results by comparing them to the data presented by NASA[2]. Then simulated various cases. We chose a suitable grid, boundary conditions, and initial conditions for the simulation process. Afterwards, we employ Paraview for post-processing the results. Our findings reveal a strong correspondence between our simulation outcomes and the literature data, affirming the accuracy of our model. Overall, our study yields results that closely align with both analytical predictions and existing literature.

**Keywords:** CFD, Prandtl-Meyer Expansion, PRAVAH, Fortran

## 1. Introduction

Ever since humanity has breached the speed of sound, one of the foremost challenges encountered upon reaching this milestone was the generation of shock waves, expansion fans etc. In this current study, an examination of Prandtl-Meyer expansion around a 15-degree convex corner has been undertaken to explain flow dynamics. Expansion shocks are significant in high-speed aerodynamics, particularly in supersonic and hypersonic flow regimes[4]. They occur when a flow expands around a convex corner or a body, leading to changes in flow properties such as pressure, density, and velocity. Understanding and controlling expansion shocks are essential for designing efficient and stable aerodynamic structures, such as aircraft wings and nose cones. Expansion shocks interact with other shock waves, such as compression shocks, leading to complex flow phenomena. These interactions are crucial in scenarios like shock-boundary layer interactions and shock-wave/boundary-layer interactions, which are encountered in high-speed aerodynamics, propulsion systems, and re-entry vehicles. Studying expansion shocks helps engineers predict and mitigate the effects of these interactions, improving the performance and safety of aerospace systems. These expansion shocks are also encountered in the exhaust flow of propulsion systems, such as rocket nozzles and jet engines. The expansion of high-pressure, high-temperature gases through a nozzle generates expansion shocks, which affect thrust performance and flow efficiency. Optimizing nozzle designs and understanding shock interactions in exhaust flows are essential for improving the efficiency and performance of propulsion systems.

The usage of numerical simulation in research is more often used to study the behaviour of any physics of flow. especially simulations help predict fast-moving flows, allowing engineers and researchers to visualize complex flow behaviors that are difficult or impossible to observe experimentally. CFD(Computational Fluid Dynamics) enables engineers to iterate and optimize designs of high-speed vehicles, aircraft, and propulsion systems without the need for costly and time-consuming physical prototypes. By simulating different design configurations and operating conditions, engineers can identify optimal shapes, control strategies, and flow control mechanisms to improve performance, efficiency. CFD simulations are often used in conjunction with experimental data to validate models and hypotheses, providing a comprehensive understanding of high-speed flow phenomena. The current study employs the Fortran (Formula Translation) language for modeling Prandtl Meyer flow, chosen for its superior performance, mathematical expressiveness, extensive numerical libraries, stability, and robust community support compared to alternative coding options.

## 2. PRAVAH

PRAVAH EDU is an educational version of the PRAVAH-3D code, developed by Dr. Rajesh Ranjan ([rajeshr@iitk.ac.in](mailto:rajeshr@iitk.ac.in)). It utilizes finite differencing schemes to solve the 2D compressible Navier-Stokes equations.

It provides flow solutions for a single structured curvilinear mesh. This mesh is transformed into an orthogonal computational mesh with unit spacing, where most calculations are performed, and then transformed back. The codes are fully parallelized using MPI, with subgrids of approximately equal size assigned to individual processors. Each processor performs computations for its subgrid, and solutions are reassembled on the full grid.

The flow solver employs a 3rd order accurate Strong Stability Preserving Runge-Kutta temporal scheme. Inviscid and viscous fluxes are solved independently. A Roe scheme with 3rd order MUSCL reconstruction calculates inviscid fluxes, with limiters from Van Leer and Van Albada used to avoid spurious oscillations. Viscous fluxes are calculated using a 2nd-order central difference scheme.

## 3. Prandtl meyer expansion fan

Prandtl-Meyer expansion refers to the phenomenon of expansion of a supersonic flow around a convex corner, such as the trailing edge of an airfoil or a corner in a duct. It is named after Ludwig Prandtl and Theodor Meyer, who made significant contributions to the understanding of supersonic flow. Prandtl-Meyer expansion is associated with the formation of expansion waves, which are compression-free waves that arise due to the gradual increase in flow velocity in the expansion region. The expansion causes the flow streamlines to diverge, leading to a change in flow direction shown in Figure 1.

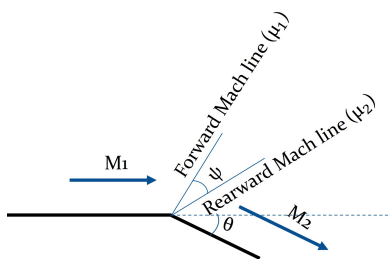


**Figure 1.** Expansion fan

These waves form a series of expansion waves. The foremost one is called the Forward Mach line, denoted as  $\mu_1$ , while the final expansion wave is termed the Rearward Mach line, denoted as  $\mu_1$ .

The angle between them is referred to as the Fan expansion angle, denoted as  $\psi$ .

$$\psi = \mu_1 - \mu_2 + \theta \quad (1)$$

These Mach lines angles can be calculated based on their Mach numbers.

$$\mu = \sin^{-1} \left( \frac{1}{M} \right) \quad (2)$$

The Prandtl-Meyer expansion angle ( $\nu$ ) quantifies the amount by which the flow is deflected due to the expansion. During Prandtl-Meyer expansion, there is no heat addition or removal from the flow, and no work is done on or by the flow. Therefore, the expansion process is isentropic, meaning it occurs without any change in entropy.

Prandtl-Meyer expansion plays a crucial role in various engineering applications, including aerodynamics, gas dynamics, and propulsion systems. Understanding and controlling Prandtl-Meyer expansion is essential for optimizing the performance of supersonic and hypersonic vehicles, as well as for designing efficient airfoil shapes and flow control devices.

The angle by which the flow direction changes due to the expansion is known as the Prandtl-Meyer angle, denoted by  $\nu(M)$ . The Prandtl-Meyer function relates the Mach number of the flow to the Prandtl-Meyer angle. The formula for the Prandtl-Meyer function is given by:

$$\nu(M) = \sqrt{\frac{\gamma+1}{\gamma-1}} \arctan \sqrt{\frac{\gamma-1}{\gamma+1} (M^2 - 1)} - \arctan \sqrt{M^2 - 1} \quad (3)$$

where,  $\gamma$  is the ratio of specific heats (also known as the adiabatic index),  $M$  is the Mach number of the flow.

The change in the Prandtl-Meyer angle ( $\Delta\nu$ ) corresponds to the change in the flow direction caused by the expansion. This change in flow direction is what we refer to as the deflection angle ( $\theta$ ). Therefore, we can express the deflection angle as the difference between the Prandtl-Meyer angles at the Mach numbers  $M_1$  and  $M_2$ .

$$\theta = \nu(M_2) - \nu(M_1) \quad (4)$$

The expansion wave is isentropic; hence,  $p_0$  and  $T_0$  are constant through the wave. That is,  $p_{02} = p_{01}$  and  $T_{02} = T_{01}$

$$\frac{T_2}{T_1} = \frac{\left(\frac{T_2}{T_{02}}\right)}{\left(\frac{T_1}{T_{01}}\right)} = \frac{1 + \frac{\gamma-1}{2} M_1^2}{1 + \frac{\gamma-1}{2} M_2^2} \quad (5)$$

$$\frac{\rho_2}{\rho_1} = \frac{\left(\frac{\rho_2}{\rho_{02}}\right)}{\left(\frac{\rho_1}{\rho_{01}}\right)} = \left( \frac{1 + \frac{\gamma-1}{2} M_1^2}{1 + \frac{\gamma-1}{2} M_2^2} \right)^{\frac{1}{(\gamma-1)}} \quad (6)$$

$$\frac{p_2}{p_1} = \frac{\left(\frac{p_2}{p_{02}}\right)}{\left(\frac{p_1}{p_{01}}\right)} = \left( \frac{1 + \frac{\gamma-1}{2} M_1^2}{1 + \frac{\gamma-1}{2} M_2^2} \right)^{\frac{\gamma}{(\gamma-1)}} \quad (7)$$

The variation of temperature, pressure, and density across expansion waves can be found from the above isentropic relations.

## 4. Numerical Methodology

### 4.1 Governing Equations

Continuity Equation

$$\frac{\partial \rho}{\partial t} + \frac{\partial}{\partial x}(\rho u) + \frac{\partial}{\partial y}(\rho v) = 0 \quad (8)$$

Momentum Equations

$$\frac{\partial \rho u_i}{\partial t} + \frac{\partial}{\partial x_j}(\rho u_i u_j) = -\frac{\partial p}{\partial x_i} + \frac{\partial \sigma_{ij}}{\partial x_j} \quad (9)$$

$$\frac{\partial \rho u}{\partial t} + \frac{\partial}{\partial x}(\rho u^2) + \frac{\partial}{\partial y}(\rho uv) = -\frac{\partial p}{\partial x} + \mu \nabla^2 u + \frac{1}{3} \mu \nabla \cdot u \quad (10)$$

$$\frac{\partial \rho v}{\partial t} + \frac{\partial}{\partial x}(\rho uv) + \frac{\partial}{\partial y}(\rho v^2) = -\frac{\partial p}{\partial y} + \mu \nabla^2 v + \frac{1}{3} \mu \nabla \cdot u \quad (11)$$

Energy Equation:

$$\frac{\partial \rho E}{\partial t} + \frac{\partial}{\partial x_j}(\rho u_j H) = \frac{\partial}{\partial x_j}(u_i \sigma_{ij}) - \frac{\partial q_j}{\partial x_j} \quad (12)$$

$$\frac{\partial \rho E}{\partial t} + \frac{\partial(\rho u H)}{\partial x} + \frac{\partial(\rho v H)}{\partial y} = \frac{\partial}{\partial x}(u \sigma_{xx} + v \sigma_{xy} - q_x) + \frac{\partial}{\partial y}(u \sigma_{xy} + v \sigma_{yy} - q_y) \quad (13)$$

Non-dimensional Form

$$\frac{\partial}{\partial t} \begin{bmatrix} \rho \\ \rho u \\ \rho v \\ \rho E \end{bmatrix} + \frac{\partial}{\partial x} \begin{bmatrix} \rho u \\ \rho u^2 + p \\ \rho uv \\ (\rho E + p)u \end{bmatrix} + \frac{\partial}{\partial y} \begin{bmatrix} \rho v \\ \rho uv \\ \rho v^2 + p \\ (\rho E + p)v \end{bmatrix} = \frac{1}{Re} \left( \frac{\partial}{\partial x} \begin{bmatrix} 0 \\ \sigma_{xx} \\ \sigma_{xy} \\ \sigma_{xx}u + \sigma_{xy}v - q_x \end{bmatrix} + \frac{\partial}{\partial y} \begin{bmatrix} 0 \\ \sigma_{xy} \\ \sigma_{yy} \\ \sigma_{xy}u + \sigma_{yy}v - q_y \end{bmatrix} \right)$$

### 4.2 Numerical Approach

#### 4.2.1 Initial Condition

The initial condition refers to the state of the flow variables (such as velocity, pressure, temperature, density, etc.) at the beginning of the simulation or computation domain. It provides the starting point for the numerical solution of the governing equations that describe fluid flow. This problem will be analyzed as a transient one, using a uniform flow as initial condition. The density, velocity components, and pressure values are set to

$$\rho = 1 \quad u = \cos 15^\circ, \quad v = \sin 15^\circ, \quad p = \frac{1}{\gamma M^2} = 0.1142 \quad (14)$$

The values are non dimensionalized with respective to their reference scale. Non-dimensionalization helps in normalizing physical quantities, which simplifies the equations and makes them easier to handle. It reduces the number of independent parameters in the equations, also helps in identifying similarity parameters that can be used to generalize results across different flow conditions. This helps in identifying the most critical dimensionless parameters governing the flow behavior and allows for a more focused analysis of the problem.

**Table 1.** Normalization of Variables

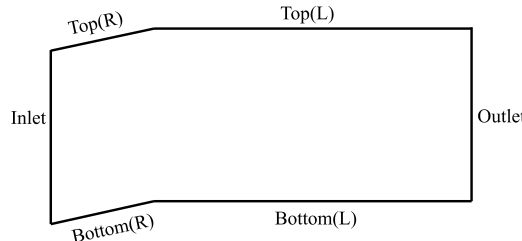
Variable	Normalized
$\hat{x}_i$	$x_i/L$
$\hat{u}_i$	$u_i/u_\infty$
$\hat{\rho}$	$\rho/\rho_\infty$
$\hat{p}$	$p/\rho_\infty u_\infty^2$

#### 4.2.2 Boundary Condition

Inlet: At the inlet, Dirichlet boundary conditions have been applied. Where we declared the primitive variables such as density, U velocity, V velocity and the pressure shown in equation (14). These are then converted into conserved variables. Bottom: The bottom of the wall has been divided into two parts Left(L) ( $X \leq 0.5$ ) and Right(R) ( $0.5 \leq X \leq 2$ ). Here in both places Dirichlet boundary conditions(Slip wall) have been applied. In the Bottom(R) face, the value of the primitive variables are from the cell just above. In the Bottom(L) face all the primitive variables are copied from the cell just above except for the third primitive variable (V velocity), here it's set to zero. This is mainly here the problem is inviscid and slip wall condition. At the outlet, Top(R) and Top(L) Neumann boundary conditions have been applied since they are far from the flow.

**Table 2.** Boundary conditions

Dirichlet BC	Neumann BC
Inlet	Outlet
Bottom(R)	Top(R)
Bottom(L)	Top(L)

**Figure 2.** Applied boundary conditions

#### 4.3 Time stepping using SSP Runge-Kutta temporal scheme

The Runge-Kutta method is a popular numerical technique for solving ordinary differential equations, which are the discrete counterparts of the continuous governing equations in CFD. The Strong Stability Preserving (SSP) variant of the Runge-Kutta method is designed to maintain stability, especially for hyperbolic PDEs like those encountered in fluid dynamics[1]. It ensures that the numerical solution remains stable even for large time steps, which is crucial for efficient and accurate simulations. In the present work, flow solver utilizes a 3<sup>rd</sup> order accurate Strong Stability Preserving Runge-Kutta temporal scheme. This is a three-stage explicit scheme which is Total Variation Diminishing (TVD).

The partial derivative of  $q$  with respect to  $t$  is given by:

$$\frac{\partial q}{\partial t} = f(q) \quad (15)$$

Three-stage explicit Runge–Kutta schemes have the form:

$$q_{n+1} = q_n + \Delta t \sum_{i=1}^3 b_i k_i \quad (16)$$

where the individual stages are given by:

$$\begin{aligned} k_1 &= f(q_n) \\ k_2 &= f(q_n + \Delta t(a_{21}k_1)) \\ k_3 &= f(q_n + \Delta t(a_{31}k_1 + a_{32}k_2)) \end{aligned}$$

The coefficients for the Strong Stability Preserving Runge–Kutta scheme are given below:

$$\begin{aligned} a_{21} &= 1, & a_{31} &= \frac{1}{4}, & a_{32} &= \frac{1}{4}, \\ b_1 &= \frac{1}{6}, & b_2 &= \frac{1}{6}, & b_3 &= \frac{2}{3}. \end{aligned}$$

#### 4.4 Roe scheme

The Roe scheme, coupled with third-order MUSCL (Monotone Upstream-Centered Schemes for Conservation Laws) reconstruction, constitutes a robust numerical method employed for computing inviscid fluxes in computational fluid dynamics (CFD) simulations [3]. The core principle of the Roe scheme involves the approximate solution of the Riemann problem at each cell interface, facilitating the calculation of fluxes across these interfaces.

The third-order MUSCL reconstruction technique enhances the accuracy of the solution by extrapolating the cell-centered values to the cell faces. This extrapolation is performed using a weighted linear combination of neighboring cell values, thereby capturing sharp gradients and discontinuities more accurately than lower-order schemes. However, third-order MUSCL reconstruction can lead to spurious oscillations, particularly near discontinuities, unless appropriate measures are taken.

To mitigate these oscillations, limiters proposed by Van Leer and Van Albada are incorporated into the reconstruction process. These limiters constrain the slopes of the reconstructed profiles, preventing excessive oscillations while maintaining the overall accuracy of the solution. By limiting the excessive steepness of the reconstructed profiles, these techniques effectively suppress numerical artifacts and ensure the stability and robustness of the numerical scheme.

#### 4.5 MUSCL Scheme

MUSCL (Monotone Upwind Schemes for Conservation Laws) and WENO (Weighted Essentially Non-Oscillatory) schemes are important in Computational Fluid Dynamics (CFD) and other areas of computational physics for several reasons

$$[q_{K+1/2}^L = q_K + \frac{\sigma_0}{4}[(1 - \sigma_1)(q_K - q_{K-1}) + (1 + \sigma_1)(q_{K+1} - q_K)]] \quad (17)$$

$$[q_{K+1/2}^R = q_K - \frac{\sigma_0}{4}[(1 + \sigma_1)(q_K - q_{K-1}) + (1 - \sigma_1)(q_{K+1} - q_K)]] \quad (18)$$

These equations might represent a discrete time dynamical system. The variable  $q_k$  likely refers to the state of the system at time step  $k$ . The terms  $q_{K+1/2}^L$  and  $q_{K+1/2}^R$  could represent left and right

sided approximations of the state at time step  $k + 1/2$ . The parameter  $\sigma_0$  controls the influence of the past states  $(q_{K-1}, q_K)$  on the future states  $(q_K, q_{K+1})$ . The parameter  $\sigma_1$  determines the relative weight given to the left and right sided approximations of the future state  $(q_{K+1/2})$ .

#### 4.6 Limiters

Van Leer's limiter is a slope limiter used in numerical methods like the MUSCL scheme to maintain monotonicity and reduce numerical oscillations.

$$r = \frac{q_K - q_{K-1}}{q_{K-1} - q_K} = \frac{\nabla q}{\Delta q} \quad (19)$$

$$\nabla q^{\text{lim}} = \nabla q \cdot \left( \frac{r + |r|}{1 + |r|} \right) \quad (20)$$

$$\Delta q^{\text{lim}} = \Delta q \cdot \left( \frac{1/r + |1/r|}{1 + |1/r|} \right) \quad (21)$$

where  $r$  is a measure of the slope of the solution. Van Leer's limiter works as follows: When  $r > 0$ , the limiter allows positive slopes, preserving the original slope. When  $r < 0$ , it suppresses negative slopes to zero, preventing undershoots. At  $r = 0$ , it maintains a constant value.

This limiter effectively prevents overshoots and undershoots, ensuring monotonicity in the solution.

Van Albada's limiter is another slope limiter used in numerical methods like the MUSCL scheme to maintain monotonicity and reduce numerical oscillations

$$\nabla q^{\text{lim}} = \nabla q \cdot \left( \frac{r^2 + r}{r^2 + 1} \right) \quad (22)$$

$$\Delta q^{\text{lim}} = \Delta q \cdot \left( \frac{1/r^2 + 1/r}{1/r^2 + 1} \right) \quad (23)$$

The adjusted gradients calculated above should then be used in the MUSCL interpolation in place of the original gradients.

#### 4.7 Computational Domain and Grid

In this current work, the grid domain has been set from the  $X_{\min} = 0$  to  $X_{\max} = 2$ , in the vertical from  $Y_{\min} = 0$  to  $Y_{\max} = 1$ . From  $X = 0$  to  $X = 0.5$  there is a 15-degree slope after which the grid becomes parallel to the horizontal. This mimics the 15-degree convex corner at  $X = 0.5$ . The selection of such a grid gave us the freedom to choose initial conditions and bottom wall conditions throughout the domain. The grid spacing in the x-axis is 0.006, while in the y-axis is 0.003 making the fine mesh in the y direction. shown in figure 4.

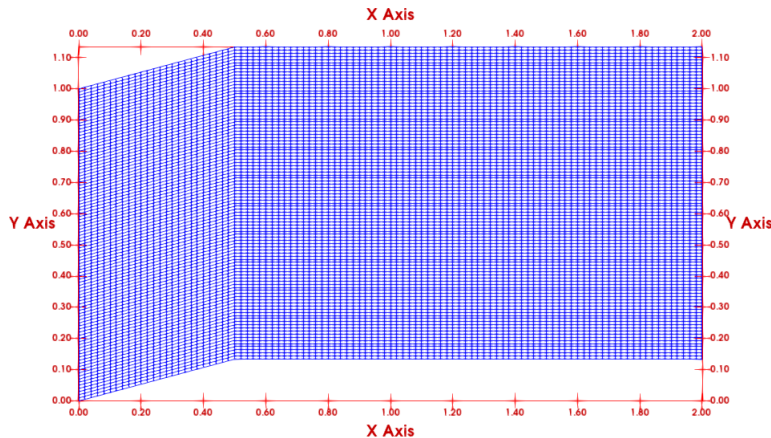


**Figure 3.** Computational grid used for the simulation

#### 4.8 Grid Convergence

In numerical simulations, the accuracy of the results depends on the convergence of the system of equations. In this study, convergence was achieved after approximately 13,000 iterations. Grid sizes ranged from 0.02 to 0.003. For better resolution, a finer mesh size of 0.003 was chosen for the simulation.

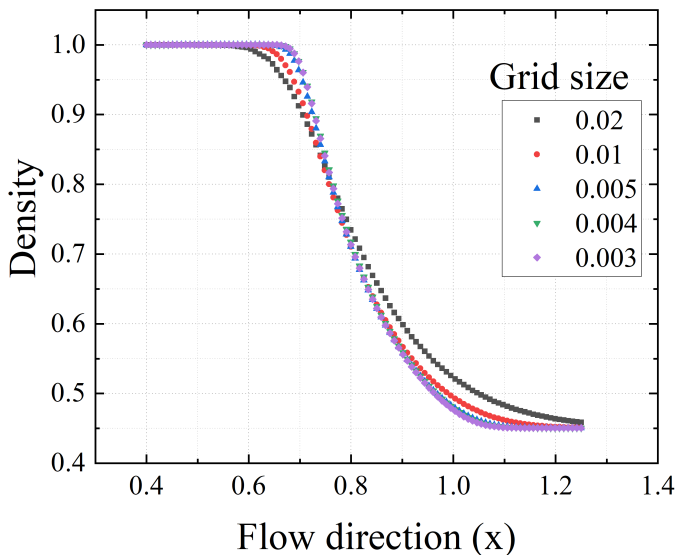


**Figure 4.** Grid independent test

### 5. Verification and validation

#### 5.1 Mach number

In the flow domain, the given Mach number 2.5 is initially flowing in the straight, when the expansion corner is met at  $x=0.5$  series of expansion waves forming at the expansion wedge, since this expansion is isentropic in nature the flow is getting accelerated as we can see from Figure ?? that the match number increasing suddenly near the corner thus resulting a further increased flow in

the downstream. This is shown in figure 5 different color schemes indicates different mach number gradient. The obtained results can be compared against the analytical data available in the table ???. The expansion mach number downstream of the flow obtained from simulation is 3.23662 the analytical mach number is 3.2368. The code predicted the mach number accurately.

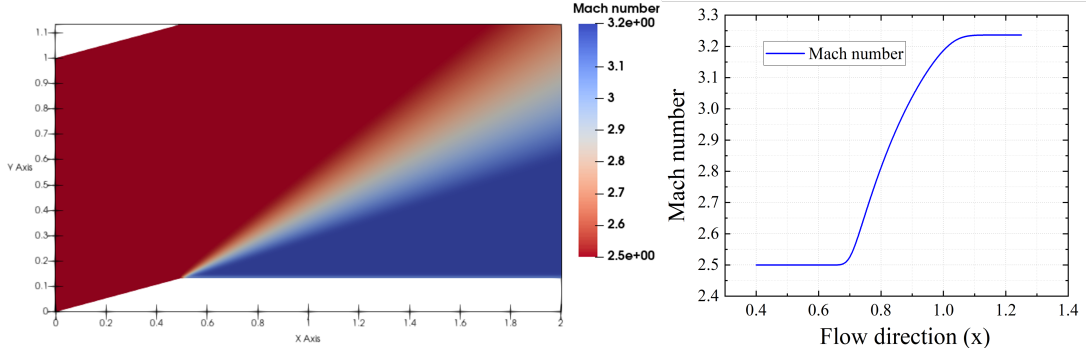


**Figure 5.** Mach number variation

## 5.2 Density

The density gradient of the wave past  $15^\circ$  is illustrated in Figure 6. Within the expansion, the highest density registered is 1, while the lowest density is 0.4315. As elaborated in Section 2, in the case of compressible flow around an expansion corner, the velocity increases, leading to a compression of downstream air, resulting in decreased density. Our analysis aligns with this phenomenon. The ratio of downstream to upstream densities ( $\rho_2/\rho_1$ ) is 0.4315. A comparison between these results and the analytical solution presented in Table ?? shows a close correspondence, with a deviation of merely 4.217/

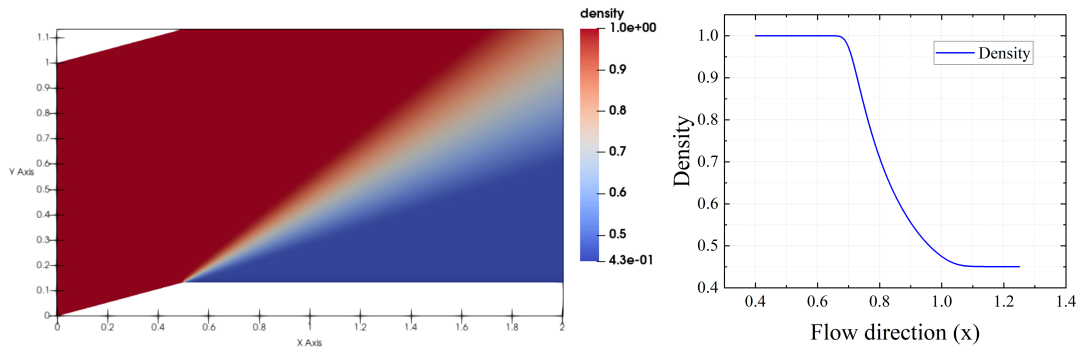


**Figure 6.** Non-dimension density variation

## 5.3 Pressure

The pressure gradient is illustrated in Figure 7. At the upstream end, the maximum pressure is 1, while the predicted downstream pressure is 0.037428. The ratio of upstream to downstream pressure ( $P_2/P_1$ ) is calculated as 0.32745. This ratio further confirms the expected phenomenon: as supersonic flow traverses an expansion corner, velocity escalates while pressure diminishes. To validate our predicted ratio, we compared it with the pressure ratio obtained through analytical calculation. The disparity between our predicted value and the analytical solution closely aligns with our results.

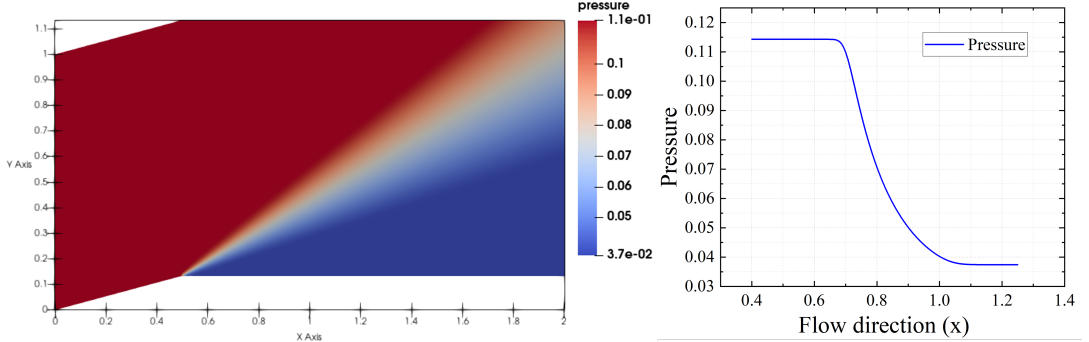


Figure 7. Non-dimension pressure variation

#### 5.4 Temperature

The Temperature gradient is illustrated in Figure 8. The ratio of upstream to downstream pressure ( $T_2/T_1$ ) is calculated as 0.7614. This ratio further confirms the expected phenomenon: as supersonic flow traverses an expansion corner, velocity escalates while pressure decreases and thus temperature decreases. To validate our predicted ratio, we compared it with the temperature ratio obtained through analytical calculation, with a deviation of merely 4.746%. The disparity between our predicted value and the analytical solution closely aligns with our results.

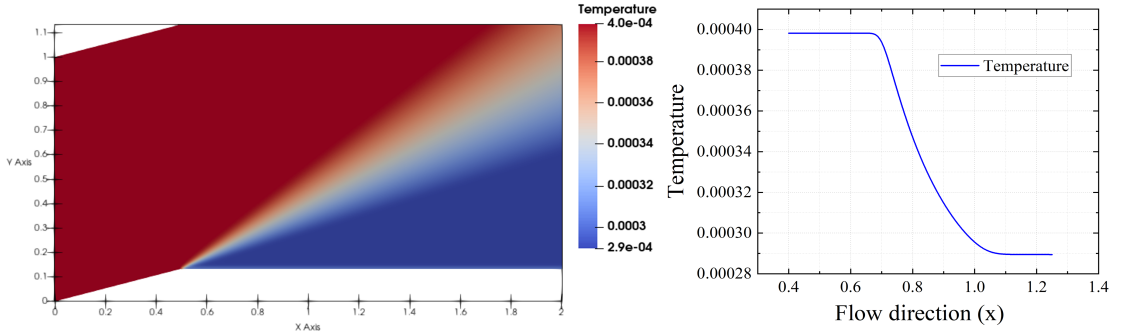


Figure 8. Non-dimension temperature variation

#### 5.5 Comparison with literature

Table 3. Comparison of Analytic, AEROFLO-MUSCL, AEROFLO-WENO, WIND, and PRAVAH

	Analytic	AEROFLO-MUSCL		AEROFLO-WENO		PRAVAH	
	Value	Value	% Error	Value	% Error	Value	% Error
$M_2$	3.2368	3.2344	0.06	3.04866	5.81	3.23662	< 0.01
$P_2/P_1$	0.32745	0.327432	< 0.01	0.32727	0.04	0.32742	< 0.01
$T_2/T_1$	0.7269	0.727607	0.08	0.77687	6.87	0.7269	< 0.01
$\rho_2/\rho_1$	0.4505	0.450012	0.07	0.42127	6.49	0.4315	4.217

The current work shows that the PRAVAH capability of predicting the Prandtl Meyer expansion waves very well. Making this code reliable for expansion wave calculations. As We compared the results with Analytical data, schemes such as the MUSCL scheme and the WENO scheme. The

Mach Number and pressure error percentage are negligible however the temperature and density have considerable errors even though it is below 5 %.

### 5.6 Fan expansion angle

The fan expansion angle between the forward machine and the rearward machine has been measured from the point at which there is a significant change in Mach number exist. Figure 9 shows the fan expansion angle for the incoming Mach 2 with wedge angle 15°. The analytical fan expansion angle is measured using the relation (3). The comparison is shown in table 4. It can be clear that the PRAVAH code has predicted the same as analytical calculation with just 3.3 % error margin.

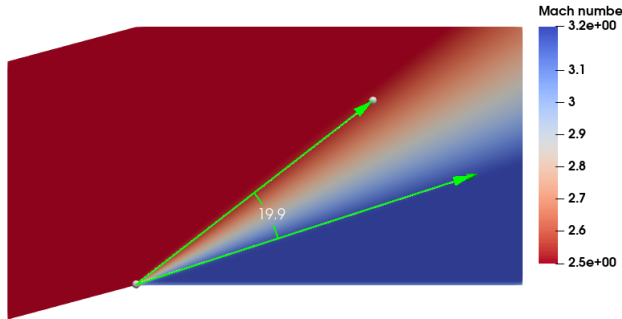


Figure 9. Fan expansion angle

Table 4. Fan expansion angle comparision

Analytical	PRAVAH	Error
20.5827	19.90	3.3 %

## 6. Results and Discussions

To utilize the PRAVAH capability in predicting the Prandtl Meyer expansion fan further three more cases have been done. In case 1, The oncoming Mach number is 2 while the wedge angle is 20, in case 2, the incoming Mach number is 3 while the wedge angle is 25, in case 3, the incoming Mach number is 2 while the wedge angle is 25. To validate the obtained results the solutions were compared against the analytical calculations (3)-(7).

### 6.1 Case 1: Mach number 2 wedge angle 20

In comparison to the validation case here the Mach number has been reduced to 2 from 2.5 and the wedge angle has been increased to 20° from .15°. The PRAVAH obtained results were compared with the analytical solution and listed in table 5. From the obtained results it is clear that as the Mach number decreased the flow properties downstream decreased. But here the fan expansion angle has increased than the validation case, this is because of the increased wedge angle from 15° to 20°.

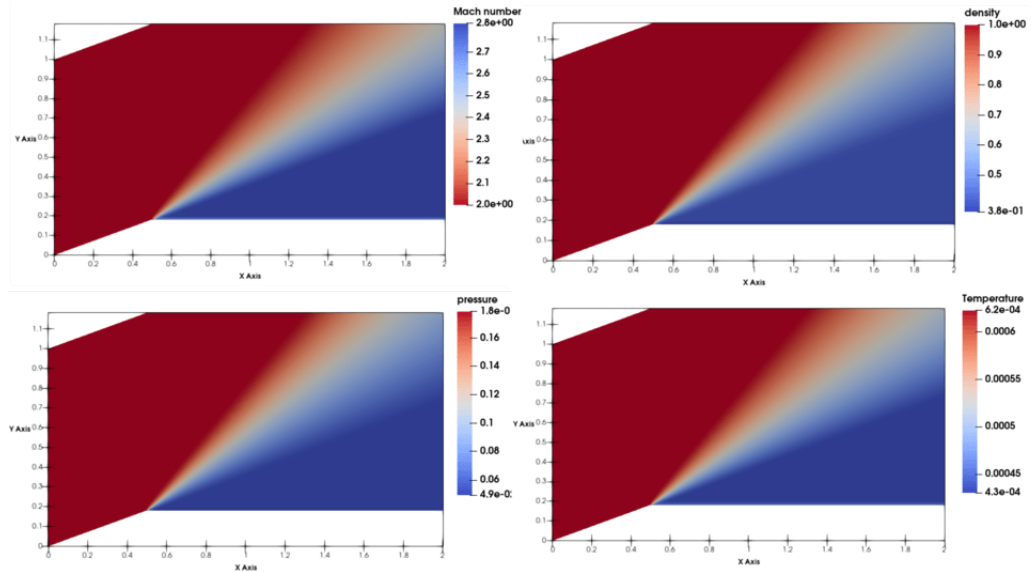


**Figure 10.** Top(R) Mach number, Top(L) Density, Bottom(R) Pressure, Bottom(L) Temperature

**Table 5.** Analytical vs PRAVAH comparison

	Analytical	PRAVAH	Error %
$M_2$	2.83	2.8304	<0.01
$\rho_2/\rho_1$	0.39785	0.37714	5.2
$P_2/P_1$	0.2751	0.27519	<0.01
$T_2/T_1$	0.69165	0.69125	<0.07
$\psi$	29.32	29.9155	<0.02

## 6.2 Case 2: Mach number 3 wedge angle 20

Here as we compare case 2 with case 1, (the Mach number increased from 2 to 3 keeping the wedge angle the same) the flow properties decreased downstream. An important observation here can be made is the decrease in the fan expansion angle when the wedge angle is kept the same, this is mainly due to the increased kinetic energy of the flow.

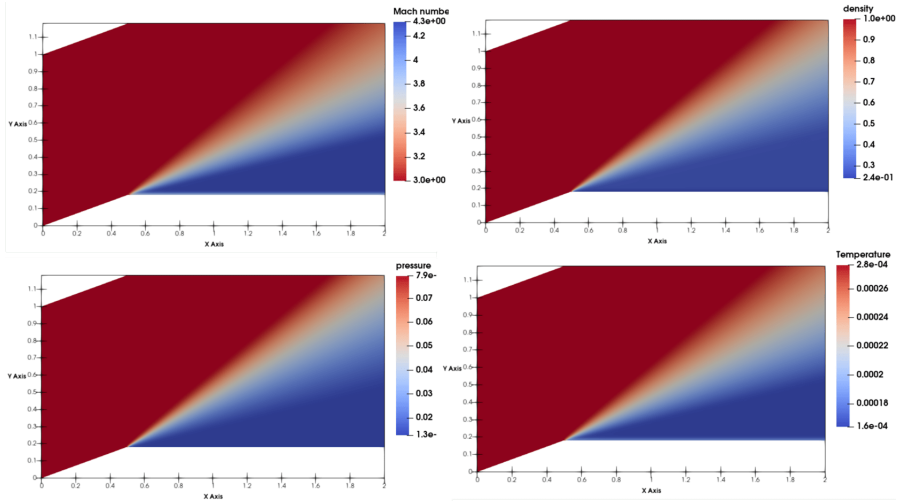


**Figure 11.** Top(R) Mach number, Top(L) Density, Bottom(R) Pressure, Bottom(L) Temperature

**Table 6.** Analytical vs PRAVAH comparison

	Analytical	PRAVAH	Error %
$M_2$	4.318332.83	4.31802	<0.01
$\rho_2/\rho_1$	0.26967	0.24039	10.8
$P_2/P_1$	0.15965	0.15966	<0.01
$T_2/T_1$	0.592016	0.5921	<0.07
$\psi$	26.0912	25.2357	<0.03

### 6.3 Case 3:Mach number 2 wedge angle 25

As we compare case 3 with case 1 (The wedge angle is increased from  $20^\circ$  to  $25^\circ$  while keeping the Mach number the same), It can be observed that the Mach number has increased and the fan expansion angle also increased. This is clear from the Prandtl Meyer function (3).

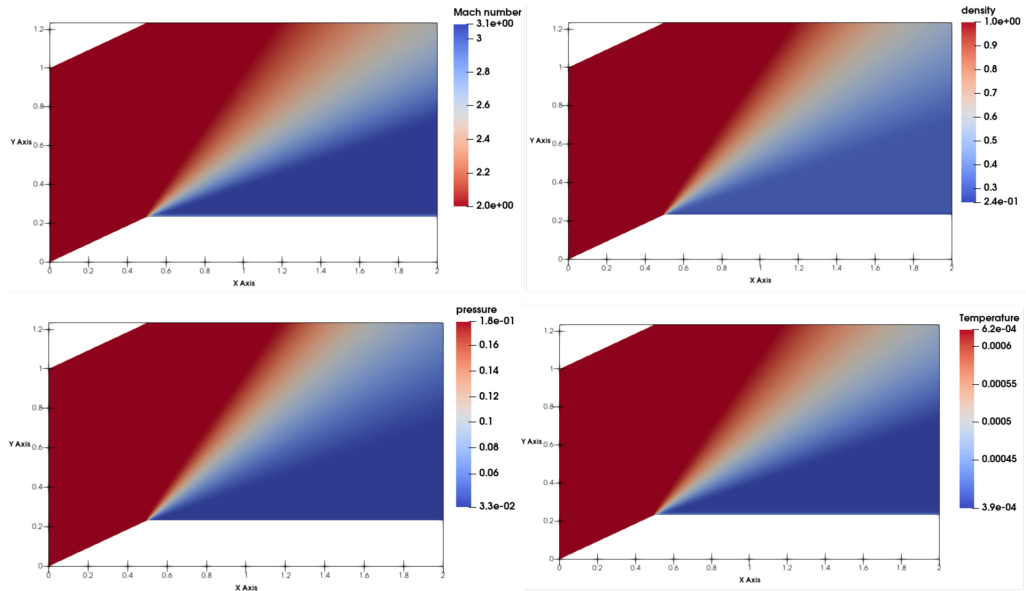


**Figure 12.** Top(R) Mach number, Top(L) Density, Bottom(R) Pressure, Bottom(L) Temperature

**Table 7.** Analytical vs PRAVAH comparison

	Analytical	PRAVAH	Error %
$M_2$	3.0855	3.0853	<0.01
$\rho_2/\rho_1$	0.30246	0.27795	8.1
$P_2/P_1$	0.187472	0.1874	<0.01
$T_2/T_1$	0.619823	0.619855	<0.01
$\psi$	36.09	35.96	<0.3

## 7. Conclusion

In the present project, the PRAVAH code was validated for its accuracy in Prandtl-Meyer expansion calculations. The obtained results were compared with existing literature and analytical calculations. The findings indicate that PRAVAH outperformed the WENO scheme with less than 5% error. Additionally, the code was modified to simulate three different scenarios by adjusting initial and boundary conditions. The results were then compared with analytical calculations, which demonstrated promising predictions of flow behavior using PRAVAH.

## References

- [1] Sigal Gottlieb, Zachary J Grant, and Liam Isherwood. “Strong Stability Preserving Integrating Factor Runge-Kutta Methods”. In: *ArXiv* (2017). arXiv: 1708.02595.
- [2] Keven Lenahan. *Contact Information*. MS 5-12, NASA Glenn Research Center. Contact: Manan Vyas, (216) 433-6053. 21000 Brook Park Road, Cleveland, Ohio, 44135.
- [3] Rajesh Ranjan. *PRAVAH EDU v3.24 Programming Guide*. Mar. 2024.
- [4] M. K. Smart and R. J. Stalker. “The glancing interaction of a Prandtl-Meyer expansion fan with a supersonic wake”. In: *The Aeronautical Journal* 95.942 (1991), pp. 39–47. doi: 10.1017/S0001924000023496.